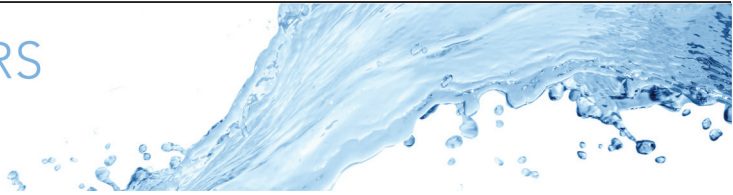




Title	Stratified horizontal convection
Author(s)	Noto, Daisuke; Ulloa, Hugo N.; Yanagisawa, Takatoshi; Tasaka, Yuji
Citation	Journal of fluid mechanics, 970, A21 https://doi.org/10.1017/jfm.2023.625
Issue Date	2023-09-10
Doc URL	http://hdl.handle.net/2115/91194
Rights(URL)	http://creativecommons.org/licenses/by/4.0
Type	article
File Information	stratified-horizontal-convection.pdf



[Instructions for use](#)



Stratified horizontal convection

Daisuke Noto^{1,†}, Hugo N. Ulloa¹, Takatoshi Yanagisawa^{2,3} and Yuji Tasaka^{2,3}

¹Department of Earth and Environmental Science, University of Pennsylvania, Philadelphia, USA

²Japan Agency for Marine-Earth Science and Technology (JAMSTEC), Yokosuka, Japan

³Laboratory for Flow Control, Faculty of Engineering, Hokkaido University, Sapporo, Japan

(Received 3 February 2023; revised 26 June 2023; accepted 26 July 2023)

Surface differential heating on a stably stratified fluid body drives an overturning circulation confined to the upper fluid region – here coined stratified horizontal convection (SHC). In this manuscript, we investigate the dynamics of SHC via laboratory experiments, exploring local and global flow properties. By considering the available potential energy of the system, we derive a unique length scale of SHC and introduce the Péclet number Pe that captures both the stabilising effect of stratification and the destabilising effect of the baroclinic adjustment. We found that Pe characterises local and global flow properties, including the fluid transport of the overturning circulation, the available mechanical energy and the flow dimensionality. Our study provides insights into the fluid dynamics of stratified environments that experience horizontal convection, such as lakes, oceans and atmospheres.

Key words: ocean circulation, stratified flows, Bénard convection

1. Introduction

Horizontal convection (HC) is a ubiquitous phenomenon (Hughes & Griffiths 2008), and it manifests across a variety of scales at which horizontal density inhomogeneity is present; large-scale circulations in the atmosphere, oceans and lakes (Wunsch & Ferrari 2004; Schneider 2006; Verburg, Antenucci & Hecky 2011; Wang, Huang & Xia 2018) land/sea diurnal breezes (Walsh 1974; Gille *et al.* 2005), heat/cool-island circulations (Lu *et al.* 1997*a,b*; Mori & Niino 2002; Niino *et al.* 2006), topographically and thermally driven flows in coastal waters (Monismith *et al.* 2006; Ulloa *et al.* 2022), radiatively driven flows in inland waters (Coates & Patterson 1993; Mao, Lei & Patterson 2009) as well as industrial casting processes (Sarris, Lekakis & Vlachos 2002; Gramberg, Howell

† Email address for correspondence: dnote@sas.upenn.edu

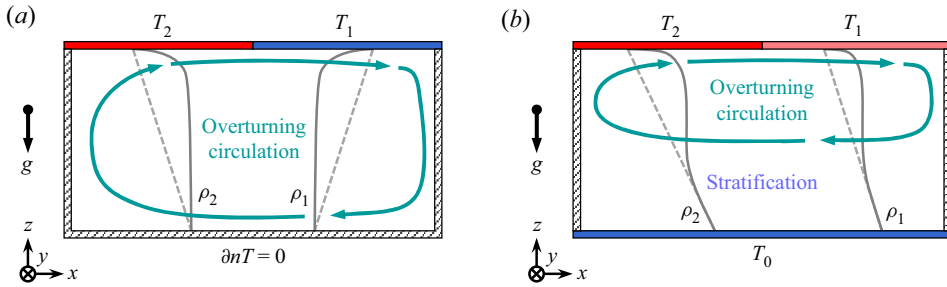


Figure 1. Schematic of (a) HC with $T_1 < T_2$ and (b) stratified horizontal convection with $T_0 < T_1 < T_2$. Thermal boundary conditions are noted. Overturning circulations are indicated by arrows. Linear density profiles imposed only by the boundary conditions are drawn by dashed lines, and the solid lines indicate mean density profiles after convective motions.

& Ockendon 2007; Chiu-Webster, Hinch & Lister 2008). Motivated by such broadly existing processes, HC continues to be investigated using the conceptual model illustrated in figure 1(a) (e.g. Wang & Huang 2005; Coman, Griffiths & Hughes 2006; Ilıcak & Vallis 2012; Shishkina, Grossmann & Lohse 2016) since the pioneering study by Rossby (1965). It is evident, however, that the traditional HC model requires additional elements to represent the complexity of actual systems, such as rotation and vertical density gradients (Couston, Nandaha & Favier 2022; Gayen & Griffiths 2022).

The traditional model of HC (figure 1a) considers a closed fluid system that is thermally insulated except on one of its horizontal surfaces, where a destabilising horizontal temperature difference, $\Delta\theta = T_2 - T_1$, is imposed. This system eventually reaches a statistical equilibrium state characterised by a basin-scale overturning circulation that penetrates the full depth of the domain and develops over the full horizontal extent. Two main dimensionless parameters govern the dynamics of this fluid system. One is the Prandtl number defined as $Pr = \nu/\kappa$, meaning the ratio of viscous diffusion to heat diffusion, where ν is the kinematic and κ the thermal diffusivity of the fluid. The other is the Rayleigh number, $Ra = u_s W/\kappa$, that quantifies the relative strength between convective and conductive heat transport within the thermally forced fluid system, with u_s and W the characteristic velocity scale of the thermally driven flow and the horizontal length scale across which thermal forcing is exerted. Conventionally, u_s is derived from a balance between buoyancy and viscous forces, i.e. $u_s = g\alpha\Delta\theta W^2/\nu$, where g and α are the gravitational acceleration and the thermal expansion coefficient. The latter leads to the classic definition of the Rayleigh number

$$Ra = \frac{g\alpha\Delta\theta W^3}{\kappa\nu}. \quad (1.1)$$

In addition, the fluid dynamics of HC is also influenced by the aspect ratio of the fluid body, i.e. $\mathcal{A} = W/H$ with H the thickness of the fluid layer. Thus, flow features, such as the heat transport and energetics, can be characterised in terms of Pr , Ra and \mathcal{A} (Hughes & Griffiths 2008; Gayen, Griffiths & Hughes 2014; Shishkina *et al.* 2016). In nature, however, fluid bodies experiencing surface differential heating/cooling – such as oceans, seas and lakes – hold a density stratification, unlike the idealised scenario above. Such a background stratification, usually controlled by a vertical temperature gradient, acts as a stabilising mechanism against destabilising buoyancy-driven fluid motions that enhance vertical mixing. Thus, when a fluid system is thermally stratified, the overturning circulation does not penetrate the depth of the basin, as illustrated in figure 1(b).

Hereafter, we call this system stratified HC (SHC), i.e. HC of a thermally stratified fluid body driven by surface differential heating. In the case of SHC, the overturning circulation develops within the uppermost fluid region. In contrast, the cooler and deeper stratified fluid remains stable and weakly energised. Notice that the dynamic response of differential cooling at the bottom surface of a thermally stratified basin is an upside-down analogue to the above scenario: the circulation is confined to the deeper region beneath the warmer and shallower stratified fluids. Intuitively, the flow features of SHC are bonded to the strength of the background stratification, characterised, for instance, by the Richardson number Ri (Peltier & Caulfield 2003), in addition to the destabilising buoyancy force ruled by Ra . Therefore, unlike in HC where the overturning circulation forms throughout the full depth, the presence of stratification exerts a confining effect in SHC, requiring the identification of the optimal vertical length scale characterising the thickness of the overturning circulation. Finding this vertical length scale from the prescribed parameters only is essential. To the best of our knowledge, the fundamental flow features of SHC depicted in figure 1(b) remain unknown. Therefore, the first sound step is building upon the current understanding of HC. As reported earlier (Scotti & White 2011; Gayen *et al.* 2013, 2014; Passaggia, Scotti & White 2017), traditional HC can reach three-dimensional (3-D) states by increasing Ra . Therefore, one can expect that SHC may also experience a transition from quasi-two-dimensional (Q2-D) to 3-D flow states for specific conditions. In fact, a transition to a 3-D state has been observed in the atmosphere as formations of clouds elongated in the flow direction at land–sea/lake borders, known as horizontal convective rolls (Lemone 1973; Weckwerth, Wilson & Wakimoto 1996; Dailey & Fovell 1999). Identifying the conditions under which such a transition occurs may provide insights into the mechanisms, energy and parameters governing the local and global fluid dynamics of SHC. Gaining this knowledge is significant for quantifying the heat and mass distributions and the ventilation of geophysical fluid environments, all critical factors influencing their ecosystem’s functioning and health. Here, we shed light on the following general questions:

- (i) What parameters control the dynamics of SHC?
- (ii) How much fluid does SHC transport?
- (iii) What flow structures can emerge in SHC?
- (iv) What mechanism controls the transition from Q2-D to 3-D states?

To address these questions, we designed and performed laboratory experiments utilising a water tank subject to steady surface differential heating and uniform cooling at its bottom boundary. The manuscript is organised as follows. In § 2, we introduce the conceptual model and the characteristic dimensionless parameters. Next, in § 3, we describe the laboratory experimental set-up. Results are reported in § 4, and we focus on describing and characterising the local and global flow features, as well as the available mechanical energy. In § 5, we discuss the mechanisms governing the formation of longitudinal rolls – the signature of the three-dimensionality. Finally, we summarise our findings in § 6.

2. Characteristic scales and dimensionless parameters

Unlike the traditional HC, the characteristic scales associated with SHC are not set by the basin aspect ratio \mathcal{A} . In the stratified scenario, the background density gradient must play a role in the controlling parameters and the dynamics of SHC. Yet, these scales are, *a priori*, unknown. Here, we derive the characteristic scales for SHC considering an Oberbeck–Boussinesq fluid with a linear equation of state, $(\rho - \rho_0)/\rho_0 = -\alpha(T - T_0)$,

where ρ is the density of the fluid. Without loss of generality, let us consider an initially thermally stratified fluid cooled from the bottom and differentially heated at its surface boundary. This scenario leads to a baroclinic adjustment owing to the horizontal density (or buoyancy) gradient developed at the surface, which ultimately drives a horizontal overturning circulation. The degree of stratification is essential in SHC as the restoring force exerted by the background stratification may substantially limit the vertical extent of the overturning circulation. In this case, the Rayleigh number (1.1) alone does not describe the fluid dynamics, as shown by Noto *et al.* (2021), and an additional parameter describing the stabilising mechanism is required. Mori & Niino (2002) investigated the progressive evolution of HC within a semi-infinite stratified domain caused by a localised cooling at the bottom. To characterise the influence of stratification on the transient flow, the authors introduced the dimensionless parameter $\Gamma' = (\partial T/\partial z)/(\Delta\theta/\ell)$ – instead of Ri . Here, $\ell = [\kappa^2/(g\alpha\Delta\theta)]^{1/3}$ is the horizontal length scale at which the baroclinic torque is prominent. The parameter Γ' describes the competition between the restoring effect of the background stratification and the destabilising effect of buoyancy, and it is time dependent until the system reaches an equilibrium state, as the vertical temperature gradient $\partial T/\partial z$ relaxes with time owing to thermal diffusion. Recently, Noto *et al.* (2021) confirmed through laboratory experiments in a closed water basin that Γ' characterises well the flow features developed by HC confined by an underlying stratification. These studies (Mori & Niino 2002; Noto *et al.* 2021) have focused only on transient processes towards equilibrium states. In the equilibrium states for a laterally confined fluid body, however, this horizontal length scale ℓ is no longer relevant since the overturning circulation takes place over the whole horizontal extent of the system W . In this sense, Γ' might help to characterise the early transient dynamics in a domain large enough such that the initial evolution of HC is not affected by the lateral boundaries. It is not straightforward to characterise the ‘effective bulk vertical temperature gradient’ in a laterally confined domain owing to the formation of the overturning circulation. Hence, in the case of closed, complex fluid environments, new characteristic scales are required to describe the fluid dynamics of SHC. In particular, for characterising the global properties of SHC, a universal dimensionless parameter should integrate bulk quantities, such as the energy available to catalyse fluid motion.

To tackle the above quest, we posit a simple question: how much energy is potentially available to sustain SHC? To address this question, we consider the available potential energy (APE) framework (Winters *et al.* 1995). In a system whose fluid parcels are out of their gravitational equilibrium positions, APE quantifies the reservoir of energy that can drive motion and enhance mixing. It is defined as the excess of potential energy that a fluid system of volume V stores relative to its state of minimum or background potential energy (BPE)

$$E_{bp} \equiv \int_V g\rho z_\star \, dV, \quad (2.1)$$

where z_\star denotes the equilibrium height of each fluid parcel of density ρ in the system. Computing BPE requires sorting of the fluid parcels adiabatically so that each fluid element is found at its height of gravitational equilibrium. Therefore, if the gravitational potential energy (GPE) of a system is $E_p = \int_V g\rho z \, dV$, with z the height of fluid parcels relative to a coordinate reference system (conventionally defined positive upward), then APE is determined by

$$E_{ap} \equiv \int_V g\rho (z - z_\star) \, dV. \quad (2.2)$$

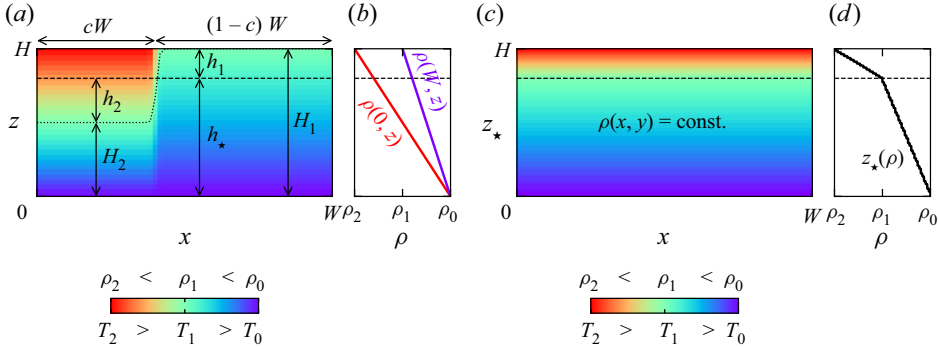


Figure 2. Schematic of adiabatic sorting: (a) linear stable stratification, (b) vertical density profiles at $x = 0$ and W , (c) minimum energy (background) state after adiabatic sorting (d) $z_*(\rho)$.

The coordinate z_* can be computed by utilising the adiabatic sorting method (Winters *et al.* 1995) or the probability density function method (Tseng & Ferziger 2001). Although the latter is more robust, we follow the former for perceptual explicitness as described in detail by Winters & Barkan (2013). Here, we summarise the key steps involved in the algorithm. First, fluid parcels are defined as discretised forms, i.e. the whole volume V is divided into a number of fluid parcels with a volume of $\Delta V(x)$ and a density of $\rho(x)$ at a position x . Second, the fluid parcels are sorted into their gravitational equilibrium positions, such that the densest fluid parcels form the deepest layer while the least dense fluid parcels form the uppermost layer. Conceptually, this adiabatic sorting is performed instantaneously, leading to a monotonically increasing density distribution from top to bottom. Third, the original shape of the parcel is modified to fit on the horizontal area of the system while keeping ΔV . That is, each fluid parcel has a height of $\Delta V/A$, where A is the horizontal cross-section of the domain. The fluid volume is eventually filled up by the ‘flattened’ parcels. Thus, we can build a one-to-one relationship between the density ρ of a fluid parcel at a position x and its equilibrium height, $z_*(x)$. The latter allows us to estimate how far (in the vertical direction) a fluid parcel is from its equilibrium height. Notice that the definition range of z_* matches exactly that of z . Figure 2 schematises the adiabatic sorting in a fluid system subject to differential heating. Let us consider the fluid body shown in figure 2(a). Its domain has a maximum height of H , a horizontal length of W and a thickness of L . The top surface is differentially heated as $T(0 \leq x < cW) = T_2$ and $T(cW \leq x \leq W) = T_1$, where $T_1 < T_2$. In contrast, the bottom surface is uniformly cooled at T_0 with $x \in [0, W]$. Here, c is an area ratio of the differentially heated surfaces, i.e. $0 < c < 1$. For the sake of simplicity, we assume that the domain is linearly stratified only in the z direction, without mixing horizontally. The vertical density profiles are drawn in figure 2(b). In this hypothetical scenario, each position x has a locally (yet not global) stable density distribution such that the horizontal density difference between the extreme lateral boundaries, i.e. $x/W = 0$ and $x/W = 1$, increases as a function of z/H . After the adiabatic sorting, the original density distribution shown in figure 2(a) transforms into the rearranged density distribution illustrated in figure 2(c). This fully stable density defines the state of minimum potential energy, i.e. the BPE. Note that density at an arbitrary horizontal slice, $\rho(x, y)$, for the background state, is constant. Thus, the APE and the BPE can be readily computed through the one-to-one relationship, $z_*(\rho)$, illustrated in figure 2(d); the APE stored in the system results by subtracting the BPE distribution (figure 2c) from the GPE distribution (figure 2a).

Here, we use the concepts of an equilibrium height and APE to characterise the physical length scales and dimensionless parameters governing SHC. In particular, we seek to find a characteristic length scale of the system, h , associated with the vertical excursion that fluid parcels with density ρ_1 perform to reach their equilibrium height h_* via the overturning circulation. In this case, the length scale can be obtained without sorting. After the adiabatic rearrangement, the fluid volume having a temperature lower than $T_1 = T_0 + \Delta T$ should be Wh_*L . This volume is identical to the sum of the fluid volume having a temperature lower than T_1 in the linearly stratified system before the sorting. Considering heights of fluid parcels having temperatures of T_1 as H_1 and H_2 in the right and left regions, respectively, the corresponding fluid volumes are easily computed as

$$V_1 = W_1 H_1 L = (1 - c)WHL, \quad (2.3)$$

and

$$V_2 = W_2 H_2 L = cW \left(\frac{\Delta T}{\Delta T + \Delta \theta} \right) HL = cW \left(\frac{1}{1 + \Theta} \right) HL. \quad (2.4)$$

Here, Θ is the ratio of the temperature differences $\Theta = \Delta \theta / \Delta T$. Considering mass conservation during the sorting, we obtain the following relationship:

$$Wh_*L = (1 - c)WHL + cW \left(\frac{1}{1 + \Theta} \right) HL. \quad (2.5)$$

Equation (2.5) yields a determination of the equilibrium height h_* as

$$h_* = \left[\frac{1 + (1 - c)\Theta}{1 + \Theta} \right] H. \quad (2.6)$$

Accordingly, fluid parcels initially at H_1 in the right region are displaced by $h_1 = H_1 - h_*$. Likewise, those parcels initially at H_2 in the left region are displaced by $h_2 = h_* - H_2$. To globally define h , these displacements are laterally averaged, giving

$$h = (1 - c)h_1 + ch_2 = 2c(1 - c) \left(\frac{\Theta}{1 + \Theta} \right) H. \quad (2.7)$$

The displacement h is a fundamental length scale of SHC and can be determined solely from prescribed parameters while considering the horizontal temperature gradient $\Delta \theta$ as a driving force and the vertical temperature difference ΔT as a braking force. Notice that h is maximised at $c = 1/2$. Here, however, c is fixed at 0.25 for all the conditions examined in this study, as explained later. The value of h can be derived irrespective of the thermal boundary conditions as long as the temperatures are prescribed – for instance, a linear horizontal temperature gradient (Rossby 1965) and more complex cases. Let us now assume that all the APE in the system is converted into the kinetic energy (KE) of the overturning circulation, i.e.

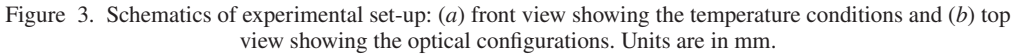
$$E_{ap} \sim E_k. \quad (2.8)$$

In the Oberbeck–Boussinesq limit, KE is defined as

$$E_k \equiv \frac{\rho_0}{2} \int_V |\mathbf{u}|^2 dV. \quad (2.9)$$

The relationship (2.8) allows linking of the characteristic length h and density anomaly characterising the APE with the advection velocity scale U_{adv} associated with the KE as

$$g\Delta\rho h \sim \rho_0 U_{adv}^2, \quad (2.10)$$


$$U_{adv} = (g\alpha\Delta\theta h)^{1/2}. \quad (2.11)$$
$$Ri \equiv \frac{N^2}{S^2} = \frac{g\alpha\Delta T/H}{(U_{adv}/H)^2} = \frac{1}{\Theta} \frac{H}{h} = \frac{1 + \Theta}{2c(1 - c)\Theta^2}. \quad (2.12)$$
$$Pe \equiv \frac{U_{adv} W}{\kappa} = \frac{(g\alpha \Delta \theta h)^{1/2} W}{\kappa} = \left(\frac{Pr Ra}{\mathcal{A} Ri \Theta} \right)^{1/2}. \quad (2.13)$$

3. Laboratory experiments

970 A21-7

$\Delta\theta$ (K)	ΔT (K)	h (mm)	U_{adv} (mm s ⁻¹)	Θ	Ra	Ri	Pe
2	0.2	22.7	8.2	10	2.3×10^8	0.293	1.7×10^4
2	1	16.7	7.0	2	2.3×10^8	2.00	1.4×10^4
2	10	4.2	3.5	0.2	2.3×10^8	80.0	7.2×10^3
10	0.2	24.5	19.0	50	1.2×10^9	0.054	3.9×10^4
10	1	22.7	18.3	10	1.2×10^9	0.293	3.7×10^4
10	10	12.5	13.6	1	1.2×10^9	5.333	2.8×10^4
20	0.2	24.8	27.0	100	2.3×10^9	0.027	5.5×10^4
20	1	23.8	26.5	20	2.3×10^9	0.140	5.4×10^4
20	10	16.7	22.1	2	2.3×10^9	2.00	4.5×10^4
30	0.2	24.8	33.1	150	3.5×10^9	0.018	6.8×10^4

Table 1. Experimental conditions using water ($Pr \approx 7$) as the test fluid.

Four independent heating/cooling units imposed thermal boundary conditions on the top and bottom. Each unit is formed by a copper plate whose inward-looking surface is in direct contact with the experimental fluid, whereas its outward-looking surface is bathed by temperature-controlled water. We can thus control the fluid temperature in contact with the inward-looking copper surface. In the present study, we set a ‘uniform temperature’ on the bottom, i.e. the four units have the same temperature, $T = T_0 > T_{md} \approx 4^\circ\text{C}$, with T_{md} the temperature of maximum density. In contrast, the top units are differentially heated. The first three units (from right to left) were set to be at $T = T_1 = T_0 + \Delta T$, and they heat three quarters of the top surface, $3WL/4$. On the other hand, the fourth unit was set to be at $T = T_2 = T_1 + \Delta\theta$ and heats the rest quarter of the total surface area, $WL/4$. To ensure a steep horizontal temperature gradient, we used a 4 mm thick rubber sheet to isolate the upper chambers from each other, as shown in [figure 3\(a\)](#). The horizontally asymmetric top temperature distribution is chosen to ensure a long-enough downstream region to develop the fluid motion after the steepest horizontal temperature gradient at $x \approx cW$, with $c = 1/4$. Since the rubber sheets are sandwiched by the neighbouring heating units, the temperature between the heating units varies linearly. Thus, as shown by Noto *et al.* (2021), the top surface temperature distribution can be modelled as

$$T(x, y, z = H) = T_{top}(x, y) = \underbrace{T_0 + \Delta T}_{T_1} + \frac{\Delta\theta}{2} \left\{ \tanh \left[-\frac{2(x - cW)}{d} \right] + 1 \right\}, \quad (3.1)$$

where d is the characteristic horizontal length between T_2 and T_1 . Here, we consider that the vertical temperature difference ΔT and the horizontal temperature difference $\Delta\theta$ are always positive. Under this scenario, SHC requires the following relationship:

$$T_{md} < T_0 < T_1 < T_2. \quad (3.2)$$

Notice that SHC also emerges for ‘surface cooling’ cases, when $T_{ice} < T_2 < T_1 < T_0 < T_{md}$, where T_{ice} is the freezing temperature $T_{ice} = 0^\circ\text{C}$ under atmospheric pressure. The above temperature relationships yield that the fluid lying beneath the overturning circulation is always stably stratified. In this study, we examined three different stratifications of varying strength, $\Delta T = 0.2, 1, 10\text{ K}$, with varying $\Delta\theta$. [Table 1](#) summarises the parameter space of the experiments.

We measured the velocity field via particle image velocimetry (PIV). For this, we seeded particles encapsulated thermochromic liquid crystals (TLC) into the fluid as tracers.

Thanks to their material properties and high traceability (mean diameter of $\sim 20\ \mu\text{m}$ and specific gravity of 1.01), TLC particles allow for robust PIV measurements. We emphasise that, although TLC particles enable visualising of the fluid temperature when excited by white light (Noto *et al.* 2019; Anders *et al.* 2020), we did not use them for that purpose. The set-up of the optical configuration is shown in figure 3(b). We captured images in two ways to resolve the velocity fields in different planes to thus investigate their three-dimensionality. Firstly, we visualised the x - z plane at $y = 0.5L$ (the centre of the fluid layer) using a green laser sheet and camera A, as illustrated in figure 3(b). This optical configuration enables measuring of the velocity field of the primary overturning circulation driven by the surface horizontal temperature gradient with a spatial resolution of 1 mm. Secondly, we visualised ten y - z planes across the x axis, from $x = 0.05W$ to $x = 0.95W$, every $0.10W$ interval. In this case, we used a halogen light sheet and camera B, as shown in figure 3(b). An actuator, controlled by a micro-computer, allowed the positioning of the halogen light sheet at the various measurement positions along the x axis. The two lighting systems were synchronised such that only one of them was on (and off) at a time. The ten planes were visualised in about 1 min. Thus, an entire measuring loop of the x - z plane and the ten y - z planes took approximately 1.5 min.

In the beginning, the fluid was at rest and uniformly stratified, $T(t = 0, x, y, z = 0) = T_0$ and $T(t = 0, x, y, z = H) = T_1$. Achieving the stable thermal stratification took typically ~ 2 h. Once the fluid was stratified, we imposed a horizontal (surface) temperature difference $\Delta\theta$ and started to perform quasi-instantaneous measurements every 20 min to track the fluid dynamics of SHC. Initially, the flow experienced a transient regime, yet, it reached a quasi-steady state after 1 h, irrespective of the experimental parameters. In the following, we only report and analyse the results observed after 2 h of starting the surface differential heating.

4. Results

4.1. Flow structures

We first examine the characteristic fluid dynamics of SHC. Figure 4 illustrates experimental results from two thermal forcing conditions. The top panels show the flow features in a strongly stratified environment, $Ri = 5.33$. In contrast, the bottom panels show flow features for a weakly stratified environment, $Ri = 0.14$. The left panels highlight the velocity field of the basin-scale overturning circulation on the x - z plane at $y = 0.5L$. The circulation is clockwise due to the baroclinic adjustment experienced between the warmer and the colder surface waters. The effect of stratification in the active layer where SHC takes place is striking. In a strongly stratified environment, SHC is vertically confined to a thin region near the surface, $z/H \gtrsim 0.8$, and its velocity field is predominantly horizontal. Whereas, in a weakly stratified environment, SHC covers almost half of the water column, $z/H \gtrsim 0.5$, and its velocity field can reach large vertical magnitudes. In all of the experiments, the active layer has an upper downstream region of the overturning circulation that is thinner and moves faster than the thicker lower upstream region. Beneath the active layer, the fluid is essentially quiescent and decoupled from the SHC. These flow structures are quasi-steady irrespective of the forcing conditions. Additionally, the centre and right panels in figure 4 show the normalised vorticity component in the streamwise (i.e. x) direction, $\omega_x/|\omega_y|_{\max}$ at two locations along the main axis. Here, ω_x is normalised by the maximum spanwise vorticity magnitude $|\omega_y|_{\max}$ in order to compare the strength of the secondary flows with the main circulations. The centre panels show $\omega_x/|\omega_y|_{\max}$ at $x = 0.25W$, where the maximum horizontal temperature gradient is imposed. In the

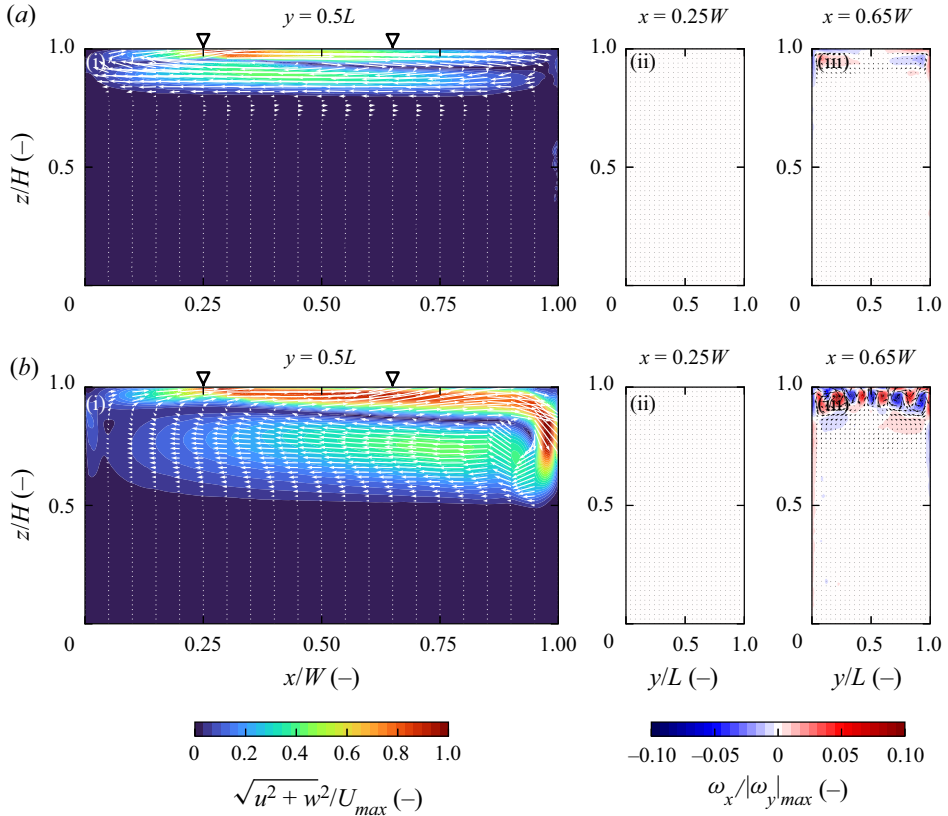


Figure 4. Flow fields measured by PIV for different conditions: (a) a strongly stratified case $Pe = 2.8 \times 10^4$ and $Ri = 5.33$ ($\Delta T = 10$ K and $\Delta\theta = 10$ K), and (b) a weakly stratified case $Pe = 5.4 \times 10^4$ and $Ri = 0.14$ ($\Delta T = 1$ K and $\Delta\theta = 20$ K). Panels (a i, b i) show the x - z planes at $y = 0.5L$ with a contour of in-plane velocity magnitude $\sqrt{u^2 + w^2}$. Panels (a ii, b ii) and (a iii, b iii) show the y - z planes at $x = 0.25W$ and $x = 0.65W$ with contours of the streamwise vorticity fields ω_x . The in-plane velocity magnitude is normalised by the maximum value U_{max} and the streamwise vorticity is normalised by the maximum of the absolute spanwise vorticity $|\omega_y|_{max}$. The reverse triangles in the panels (a i, b i) correspond to the positions of y - z planes displayed in (a ii, b ii) and (a iii, b iii). Velocity vectors shown here are reduced from the original resolution for visibility.

region $0 \leq x/W \leq 0.25$, the active layer does not exhibit vorticity, and the largest but still small magnitudes are observed near the vertical walls. The right panels show $\omega_x/|\omega_y|_{max}$ at $x = 0.65W$; here, the vorticity field has a distinctive signature, especially for those cases with weak stratification. However, for systems hosting strong stratifications, the vorticity magnitude is substantially weaker, less than 10 %, suggesting that SHC is practically two-dimensional in those cases. Regardless of the strength of the background stratification, the largest magnitudes of $\omega_x/|\omega_y|_{max}$ are found in the region $0.25 < x/W \leq 1$. In this zone, the warmer fluid transported from the upper left region $0 < x/W \leq 0.25$ gets exposed to the cooler top surface. This leads to an unstable density distribution within the upper downstream region of the overturning circulation, which fosters the development of Rayleigh–Bénard rolls in the y - z planes and vorticity production. Such a coherent vortical pattern is not identified in strongly stratified cases, suggesting that SHC can transition from Q2-D to 3-D regimes depending on the forcing conditions.

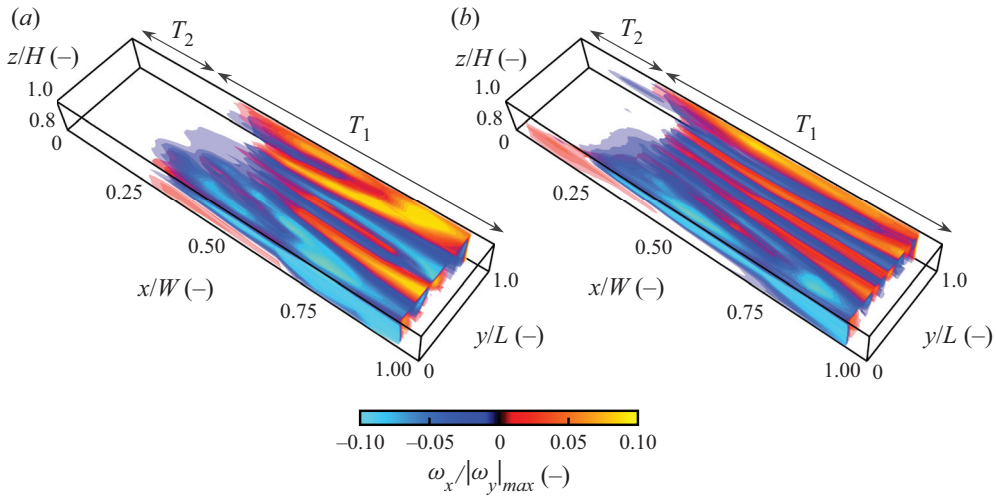


Figure 5. Isosurfaces of streamwise vorticity ω_x for the case of a 3-D flow state realised with the same $\Delta\theta$. (a) The intermediate stratification case, $Pe = 5.4 \times 10^4$ and $Ri = 0.14$ ($\Delta T = 1$ K and $\Delta\theta = 20$ K). (b) The weak stratification case, $Pe = 5.5 \times 10^4$ and $Ri = 0.027$ ($\Delta T = 0.2$ K and $\Delta\theta = 20$ K).

We examine the three-dimensionality of the flow state shown in figure 4(b) by reconstructing the spatial structure of the streamwise vorticity component, ω_x . For this, we used the PIV measurements made in the y - z plane every $0.1W$, between $x = 0.05W$ and $x = 0.95W$. Here, ω_x was interpolated between two consecutive planes for display. Figure 5 illustrates isosurfaces of $\omega_x/|\omega_y|_{\max}$ for two experiments within the upper active layer, $0.8 \leq z/H \leq 1$. Both experiments have similar Péclet numbers, $Pe = 5.4 \times 10^4$ and 5.5×10^4 , yet different Ri . Results in panels (a) and (b) are characterised by $Ri = 0.14$ and 0.027 , respectively. Notice that figure 5(a) corresponds to the case shown in figure 4(b). In both cases, ω_x emerges from the zone that hosts the maximum horizontal temperature gradient, i.e. $x/W \approx 0.25$. However, around $x/W \approx 0.3$ – 0.4 , the streamwise vorticity reveals the existence of coherent longitudinal roll structures (LRSs) that self-organise over the entire spanwise domain until the end of the basin, $x/W = 1$. The self-organisation of LRS is complex, however. Figure 5 shows that once LRSs form, their wavenumber decreases downstream due to the coalescence of adjacent rolls. The latter process is evident when comparing the number of roles at $x/W = 0.5$ and $x/W = 0.95$. In particular, we identify that the wavenumber attributed to LRS is bigger for the case with the weaker stratification, figure 5(b), than the scenario with the stronger stratification, figure 5(a). It is worth noting that LRS has significantly weaker vorticity than SHC. Indeed, the strength of LRS vorticity is approximately 10 % of that in the basin-scale overturning circulation at the most. Although earlier studies on traditional HC have reported the emergence of LRS (Mullarney, Griffiths & Hughes 2004; Gayen *et al.* 2014; Vila *et al.* 2016), their emergence and evolution in stratified environments have not been investigated in detail yet.

4.2. Fluid transport and flow regimes

The basin-scale fluid transport can be characterised by means of the streamfunction, ψ , that satisfies the Poisson equation

$$\nabla^2 \psi = \omega_y, \quad \text{with } \psi = 0 \quad \text{at the boundaries.} \quad (4.1)$$

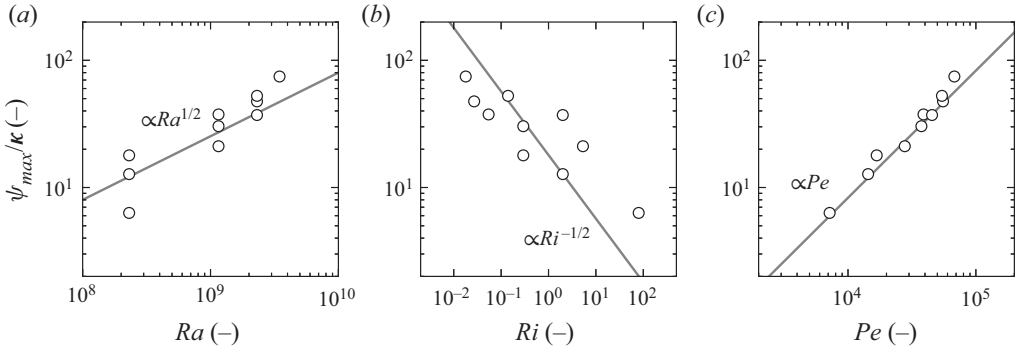


Figure 6. Maximum streamfunction ψ_{max} plotted for (a) Ra , (b) Ri and (c) Pe . Solid lines represent power-law trends.

We integrated (4.1) to resolve ψ using the successive over-relaxation method, as previously done in Noto *et al.* (2021). Here, we investigate the global transport properties of SHC by mapping ψ_{max} against dimensionless parameters introduced in § 2. Figure 6 displays the maximum streamfunction ψ_{max} normalised by the thermal diffusivity κ vs Ra , Ri and Pe , respectively. Solid lines indicate power-law trends, $\psi_{max} \propto Ra^{1/2}$, $\propto Ri^{-1/2}$ and $\propto Pe$.

As shown in figure 6(a), ψ_{max} increases with Ra , meaning that a stronger horizontal destabilising effect transports more fluid. In the case of HC, i.e. with no stable background stratification, the maximum streamfunction ψ_{max} has been found to fulfil the well-known theoretical scaling $\psi_{max} \propto Ra^{1/5}$ (e.g. Rossby 1965; Hughes & Griffiths 2008; Shishkina *et al.* 2016). The power-law trend of Ra for SHC seems stronger, as indicated by the solid line, $\psi_{max} \propto Ra^{1/2}$. There is, however, an evident deviation among experiments owing to different background stratifications, making Ra unsuitable for describing the transport associated with SHC. In contrast to the trend on Ra , ψ_{max} decreases as Ri increases, as shown in figure 6(b). This trend, $\psi_{max} \propto Ri^{-1/2}$, highlights that the strength of the overturning circulation is substantially controlled by the strength of background stratification, i.e. the stratification suppresses the convective motions. Similarly to Ra , however, Ri does not provide a unifying trend. This trend is similar to the previously obtained experimental scaling $\psi_{max} \propto \Gamma'^{-1/2}$ found by Noto *et al.* (2021), even though it was obtained for transient processes. Since the same scaling was found in different configurations, Ri defined in this study can be regarded as an analogue of Γ' defined for time-dependent differential heating of cold water bodies. Figure 6(c) illustrates a striking collapse, i.e.

$$\psi_{max} \propto Pe. \quad (4.2)$$

In fact, the best power-law fit is $\psi_{max} \propto Pe^{1.02 \pm 0.04}$. Note that the experimental results collapse to the scaling law (4.2) regardless of the flow dimensionality and the background stratification condition. Summing up, figure 6 shows that SHC transport is exceptionally characterised by Pe .

Assuming $\partial^2/\partial x^2 \ll \partial^2/\partial z^2$ in (4.1) for the boundary layer on the surface whose thickness is $\delta_v \ll W$, we get the following relationship:

$$\frac{\psi}{\delta_v^2} \sim \frac{w_c}{W} + \frac{u_c}{\delta_v}, \quad (4.3)$$

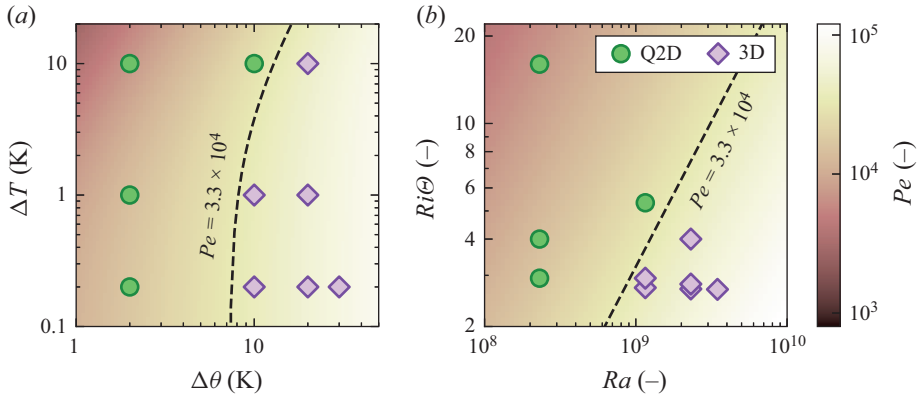


Figure 7. Regime diagram of SHC plotted for (a) the two controllable temperature differences, $\Delta\theta$ and ΔT and (b) the two dimensionless parameters, Ra and $Ri\Theta$, for $Pr \approx 7$. Colour contour represents the Péclet number Pe . Dashed line, $Pe = 3.3 \times 10^4$, is the estimated border for the two different flow regimes.

where u_c and w_c are the characteristic horizontal and vertical velocities. From the continuity, w_c is negligible as $w_c \sim (\delta_v/W)u_c$. Replacing u_c by U_{adv} , we obtain

$$\frac{\psi}{\kappa} \sim \frac{U_{adv}\delta_v}{\kappa} = \frac{\delta_v}{W}Pe. \quad (4.4)$$

Here, δ_v is considered as a depth of the maximum horizontal velocity from the surface and may vary with Ra as in HC (Hughes & Griffiths 2008). However, we confirmed that δ_v does not change much with the control parameters, and typically $\delta_v \sim 0.03H$. Thus, the maximum streamfunction can be scaled as $\psi_{max} \propto Pe^1$.

As discussed earlier, SHC exhibits two characteristic flow regimes: (i) a Q2-D overturning circulation and (ii) an overturning circulation coupled with LRSs that make the SHC fluid dynamics three-dimensional. Figure 7(a) summarises the flow regimes for the experimental conditions investigated in this study as a function of the vertical temperature difference, ΔT (vertical axis), the horizontal temperature difference, $\Delta\theta$ (horizontal axis) and Pe in the colour map. Green circles denote experiments with a Q2-D flow state, whereas violet diamonds denote experiments with a 3-D flow state. Recall that vertical and horizontal temperature gradients characterise stabilising and destabilising forcing mechanisms, respectively. Thus, from low to high horizontal temperature differences, we expect the buoyancy-driven flow to intensify and transition from 2-D to 3-D regimes fostering HC and RBC in the uppermost zone of the fluid body. In contrast, from low to high vertical temperature differences, we anticipate a reinforcement of stratification that counteracts vertical motions, resulting in a shift from a 3-D to a 2-D flow regime. This intuitive flow behaviour is actually observed in figure 7. Furthermore, since $Pe \propto Ra^{1/2}(Ri\Theta)^{-1/2}$ (see (2.13)), we can map the flow regimes into the Ra – $Ri\Theta$ space. Figure 7(b) shows that this parameter space successfully segregates the flow regimes. Empirically, it is possible to identify a border between the two flow regimes, shown by the dashed lines in figure 7. These lines characterise a unique critical Péclet number value, estimated as $Pe_c \approx 3.3 \times 10^4$, that allows describing of the flow dimensionality for SHC.

4.3. Available mechanical energy

Examining the energy distribution in SHC is relevant to understanding how the controlling parameters are tied to the production of available mechanical energy in the system. The system is forced only by the surface heating at a prescribed degree, and part of the created APE E_{ap} is transformed into KE E_k , in the form of convective motions (Winters *et al.* 1995; Winters & Barkan 2013). The parameter E_{ap} requires density distributions for computation, and these are hard to directly measure from experiments. Accordingly, we apply the temperature reconstruction method recently introduced in Noto, Ulloa & Letelier (2023), which is applicable to quasi-steady thermally driven flows under well-defined boundary conditions. Density and temperature distributions are estimated from the velocity fields by solving the heat equation

$$\frac{\partial T}{\partial t} + \mathbf{u} \cdot \nabla T = \kappa \nabla^2 T. \quad (4.5)$$

Once the system reaches an equilibrium state (after approximately 2 h from imposing $\Delta\theta$), heat advection balances heat diffusion. Although SHC supports local 3-D features for specific Pe numbers, the global overturning circulation remains two-dimensional, regardless of the Pe conditions. In this regard, a mean temperature field in the x - z plane can be reconstructed utilising PIV velocity field measurements and the steady state heat equation

$$u \frac{\partial T}{\partial x} + w \frac{\partial T}{\partial z} = \kappa \left(\frac{\partial^2 T}{\partial x^2} + \frac{\partial^2 T}{\partial z^2} \right). \quad (4.6)$$

The assumption of Q2-D flow is reasonable because the velocity component v in the y -direction is significantly smaller than those of the x and z components. To obtain a steady solution of T , we use the Dirichlet boundary conditions for the top and the bottom, and Neumann boundary conditions for the sidewalls, i.e.

$$T(x, z = 0) = T_0, \quad T(x, z = H) = T_{top},$$

$$\text{and} \quad \left. \frac{\partial T}{\partial x} \right|_{x=0} = \left. \frac{\partial T}{\partial x} \right|_{x=W} = 0, \quad (4.7a-c)$$

as temperature boundary conditions. Here, the surface temperature distribution T_{top} is estimated from (3.1). Since the heat leakage through the lateral wall estimated by the material properties is $\lesssim 4\%$ for the worst case, the adiabatic thermal boundary condition is reasonable. For the velocity field, no-slip conditions are imposed for all of the rigid boundaries, i.e. $\mathbf{u}(\mathbf{x} \in \partial V) = \mathbf{0}$. Equation (4.6) is discretised by the second-order central-difference scheme, and T is obtained throughout iterative processes of the Gauss–Seidel method. Owing to the assumption of Q2-D flow, the estimated temperature fields should be slightly different from the actual one, in particular for the 3-D flows. It, however, provides reasonable estimations of temperature distributions in the proximity of the top surface, as the magnitude of v is significantly smaller than those of u and w . Once T is computed, density distribution ρ is obtained from a linear equation of state, $\rho = \rho_0[1 - \alpha(T - T_0)]$. As explained in §2, the potential energy (PE) E_p of the system can be decomposed into BPE E_{bp} and APE E_{ap} , i.e. $E_p = E_{bp} + E_{ap}$. The BPE does not contribute to driving fluid motions but constantly restratifies the system; the BPE density

\mathcal{E}_{bp} is defined as

$$\mathcal{E}_{bp} = g\rho z_{\star}. \quad (4.8)$$

The APE, in contrast, is the energy available for fuelling SHC and enhancing mixing in the active layer. The APE density \mathcal{E}_{ap} is defined as

$$\mathcal{E}_{ap} = g(\rho - \bar{\rho})(z - z_{\star}). \quad (4.9)$$

Here, $\bar{\rho}$ corresponds to the compensatory displacements that emerge during the adiabatic sorting, and it is written as

$$\bar{\rho} = \frac{1}{z - z_{\star}} \int_{z_{\star}}^z \rho(\hat{z}_{\star}) d\hat{z}_{\star}, \quad (4.10)$$

and accordingly,

$$\mathcal{E}_{ap} = g\rho(z - z_{\star}) - g \int_{z_{\star}}^z \rho(\hat{z}_{\star}) d\hat{z}_{\star} \geq 0. \quad (4.11)$$

Notice that \mathcal{E}_{ap} is positive definite, and the second term of the right-hand side can be cancelled out by integration of the whole domain (Winters & Barkan 2013). The APE is thus computed by integrating \mathcal{E}_{ap} for the whole domain as $E_{ap} = \int_V \mathcal{E}_{ap} dV$. Considering the depth of the main overturning circulation, h , a scale of APE can be estimated for the limited volume $V' = (h/H)V$ as

$$E_{ap} \sim g\Delta\rho hV' \sim g\rho_0\alpha\Delta\theta h \left(\frac{h}{H}V\right) \propto Pe^2. \quad (4.12)$$

For the present study, E_{ap} is estimated to be $O(10^{-6}\text{--}10^{-4})$ J. The KE density, \mathcal{E}_k , is defined for each fluid parcel as

$$\mathcal{E}_k = \frac{1}{2}\rho_0|\mathbf{u}|^2 = \frac{1}{2}\rho_0(u^2 + v^2 + w^2), \quad (4.13)$$

where ρ_0 is the reference density corresponding to the bottom temperature T_0 . In contrast to \mathcal{E}_{ap} , \mathcal{E}_k is straightforward to compute as the PIV measurements allow reconstructing of full velocity fields in the 3-D domain. To obtain the global KE, \mathcal{E}_k is integrated over the whole domain as $E_k = \int_V \mathcal{E}_k dV$. In non-SHC systems, E_k is typically two orders of magnitude smaller than E_{ap} (Gayen *et al.* 2013), meaning that only a few per cent of the APE is transformed into KE to drive the horizontal overturning circulation. Figure 8 shows the spatial distributions of the streamfunction ψ , the temperature T , the KE density \mathcal{E}_k and the APE density \mathcal{E}_{ap} for the case of Q2-D state, $Pe = 2.8 \times 10^4$ and $Ri = 5.33$. The results show the existence of two basin-scale overturning cells. One is localised immediately beneath the heating surface, whereas the second cell is found directly under the shallower overturning, as shown in figure 8(a). The temperature distribution in figure 8(b) shows that the system is mostly stably stratified, except for the region hosting the most vigorous circulation (see the bending of the isotherm between $x/W \in [0.25, 0.5]$). As expected, figure 8(c) shows that \mathcal{E}_k peaks within the main overturning circulation, whereas the deep stratified region remains motionless. Consistently, \mathcal{E}_{ap} reaches a maximum in the shallow region, as shown in figure 8(d). We stress that the velocity component in the y direction is also taken into account for computing \mathcal{E}_k , yet its contribution is less than 3% at the maximum. This result shows that APE is mostly spent in stratifying the system and mixing the uppermost waters, whereas only the shallow region confined immediately beneath the heating surface is kinetically energised.

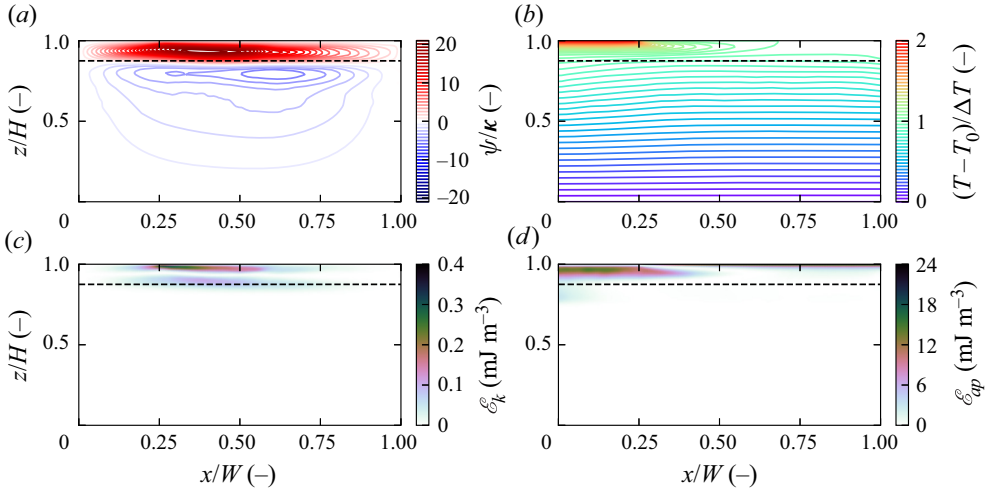


Figure 8. Spatial distributions of (a) streamfunction ψ , (b) temperature T estimated by (4.6), (c) KE ε_k and (d) APE ε_{ap} for the case of $Pe = 2.8 \times 10^4$ and $Ri = 5.33$ (Q2-D state, corresponding to figure 4a). Dashed lines indicate the theoretical estimation of the overturning circulation thickness, $z = H - h$.

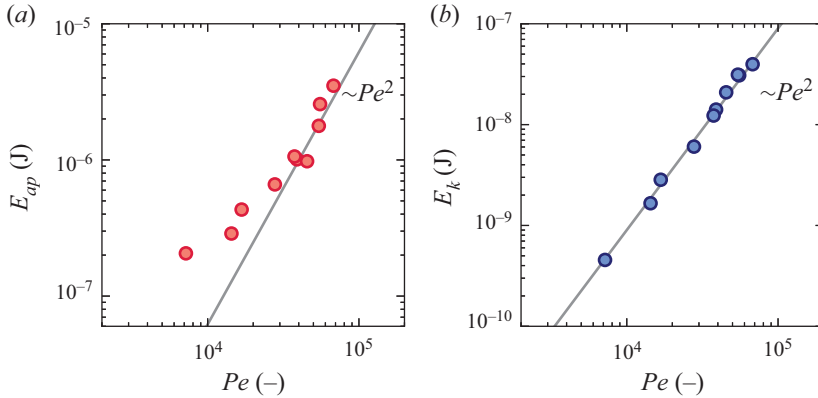


Figure 9. Mechanical energies plotted for Pe : (a) APE E_{ap} and (b) KE E_k .

Figure 9(a,b) shows the available mechanical energy components, APE and KE, vs Pe . The APE has an interesting behaviour in terms of Pe . For a Péclet number bigger than $Pe \approx 3 \times 10^4$, the APE follows the anticipated scaling (4.12) as $E_{ap} \sim Pe^2$. In contrast, for $Pe \lesssim 3 \times 10^4$, E_{ap} is less dependent on Pe . An intriguing aspect is that the evident break occurs exactly at $Pe \approx 3.3 \times 10^4$, the empirical critical Péclet number at which a shift from Q2-D to 3-D flow occurs, shown in figure 7. In other words, our results suggest that the APE has a low- Pe trend linked to a Q2-D SHC and a high- Pe trend ($E_{ap} \sim Pe^2$) associated with a 3-D SHC. Conversely, KE collapses into the line of $\sim Pe^2$. Certainly, SHC at high- Pe behaves more ‘inviscid’, meaning that the theoretical scalings for KE and APE are well captured by the advective velocity scale U_{adv} (2.11) and the length scale h (2.7) characterising an adiabatic sorting of mass in the system.

We stress that the computed KE is two orders of magnitude smaller than the APE, irrespective of Pe values. Thus, our results show that the overturning circulation is driven

Stratified horizontal convection

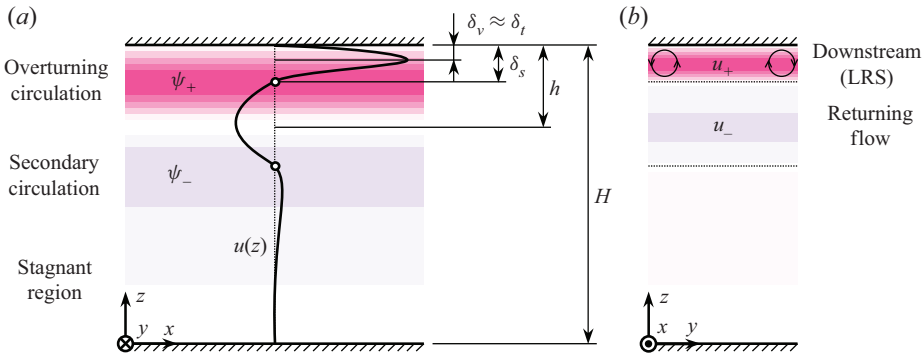


Figure 10. Overall view of flow structures and associated length scales.

only by a small part of the APE. Since the system reaches a quasi-steady state, this implies that the remainder of the APE is transformed into BPE and used to sustain the stratification via irreversible thermal diffusion. This result agrees with the energy partitioning found by Gayen *et al.* (2013) in HC, i.e. a small fraction of APE, less than 10 %, is allocated to KE.

5. Discussion

The results shown in § 4 display similarities to and differences from those in HC. To understand the fluid dynamics of SHC further, we now focus on discussing the details of the transitional flow features, LRSs and mechanical energy conversion. Since SHC posits different vertical length scales, an overall view of the flow structures is illustrated in figure 10 to clarify their relationship. The SHC exhibits structure layering from top to bottom, i.e. an overturning circulation, a secondary flow which circulates inversely to the primary circulation due to viscous coupling and a stably stratified stagnant region at the bottom. Here, we recall three length scales: h , the intrinsic vertical length scale of SHC, representing the overturning circulation depth; δ_v , the thickness associated with the viscous boundary layer at the surface and comparable to the thermal boundary layer thickness δ_t ; δ_s , the thickness of the downstream region, explained later.

5.1. Longitudinal roll structures

As demonstrated in § 4.1, Pe , the ratio of heat transport carried by convection to that owing to thermal conduction, describes well the flow features and the flow states of SHC. Therefore, we can hypothesise that 3-D flows resulting from the emergence of LRS occur when SHC cannot fully remove the heat from the highest temperature surface. Thus, a secondary flow transports heat vertically in addition to the overturning circulation. In other words, the formation of the longitudinal rolls may result from the need for extra vertical heat transport. Here, we investigate the flow structure of longitudinal rolls and their forming mechanism immediately beneath the heating surface. Vertical profiles of horizontal velocity u , temperature T , and mean absolute streamwise vorticity $\langle |\omega_x| \rangle_y$ close to the heating surface, $z/H \geq 0.8$, at the different x positions are shown in figures 11(a), 11(b) and 11(c), respectively. Here, u is measured directly by PIV and normalised by the bulk maximum horizontal velocity u_{max} . The temperature T is estimated from (4.6) using the velocity field measured by PIV and normalised by the local maximum T_{lmax} at each x position. The streamwise vorticity ω_x is computed from PIV, and its mean absolute value is derived by taking the spanwise average as $\langle |\omega_x| \rangle_y(z) = (1/L) \int_0^L |\omega_x|(y, z) dy$ at each x

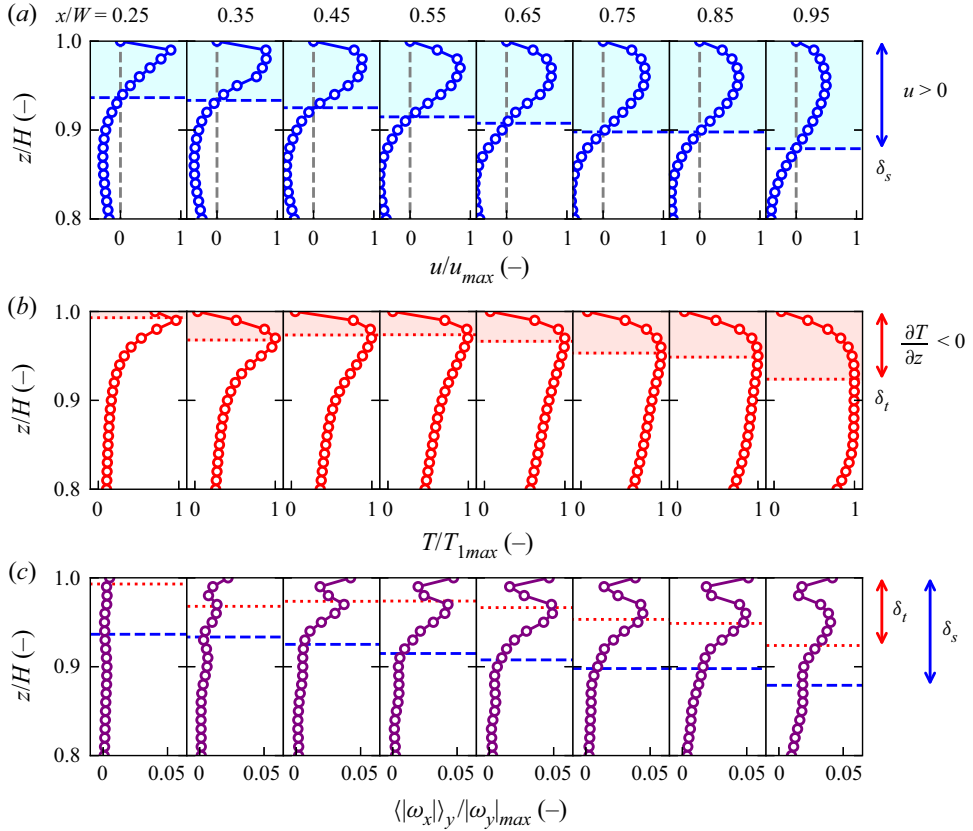


Figure 11. Detail views of the LRSs for the case of $Pe = 5.4 \times 10^4$ and $Ri = 0.14$. (a) Horizontal velocity profiles $u(z)$, (b) temperature profiles $T(z)$ and (c) mean absolute streamwise vorticity profiles $\langle |\omega_x| \rangle_y(z)$ at the different x positions. Here, u is normalised by the maximum horizontal velocity in the bulk u_{max} , and T is normalised by the local maximum T_{lmax} at each x position.

position and normalised by the maximum absolute spanwise vorticity $|\omega_y|_{max}$. Figure 11(a) highlights in light blue the shallow streaming regions at which $u > 0$. The thickness of the shallow region is expressed as δ_s , and dashed lines indicate the zero-crossing heights of u . Similarly, figure 11(b) highlights in light red the regions of unstable temperature distribution $\partial T / \partial z < 0$. The unstable layer thickness is denoted as δ_t , and the bottom of the unstable stratification, shown by dotted lines, corresponds to the local temperature maximum T_{lmax} . The above thicknesses are plotted in figure 11(c) for comparison. Positive peaks in $\langle |\omega_x| \rangle_y$ shown in figure 11(c) are recognisable at $x/W \geq 0.35$ – these peaks should be attributed to LRSs. The LRSs seem to be encompassed by the shallow streaming region of the overturning circulation as the peaks are found within δ_s . As the shallow upper region thickens downstream, so do the LRSs.

The mechanism forming LRSs in SHC can be investigated via an analogue system, the so-called Rayleigh–Bénard–Poiseuille (RBP) convection. The RBP convection is a Poiseuille flow subjected to an unstable vertical temperature gradient environment that potentially drives Rayleigh–Bénard convection. The similarity between RBP convection and SHC is illustrated in figures 12(a) and 12(b). The RBP convection has been studied especially for characterising heat transfer processes of air ducts, and an early comprehensive review for this problem is found in Nicolas (2002). A mean flow with a

parabolic (Poiseuille) velocity profile is subjected to a destabilising vertical temperature difference ΔT across the full height H_v . Accordingly, the RBP convection can be characterised by the vertical Rayleigh number, $Ra_v = g\alpha\Delta TH_v^3/(\kappa\nu)$. Note that the mean flow itself does not contribute to the development of LRSs. However, the LRS formation happens when the system is closed in the spanwise direction. The presence of the lateral walls supports the corner roll formation due to the pressure gradient at the corner, and this corner roll triggers the generation of LRSs towards the interior. As a result, LRSs are aligned in the spanwise direction (Akiyama, Hwang & Cheng 1971; Pabiou, Mergui & Benard 2005; Mergui, Nicolas & Hirata 2011; Taher & Abid 2018; Taher *et al.* 2021). Since Ra does not change along the streamwise direction, the characteristics of LRSs do not change in space under fixed environments. By contrast, in the case of SHC, the shallow streaming region of the main circulation plays a similar role to that of the main flow of RBP convection. In addition, the overturning circulation transports heat from the highest temperature surface ($0 \leq x \lesssim W_2$). This horizontal heat transport spontaneously creates an unstable temperature gradient in the downstream uppermost region, as the surface temperature is lower than that upstream. For the onset of Rayleigh–Bénard-like convection, we can define a local Rayleigh number considering the unstable layer thickness as $Ra_t = g\alpha\Delta T_t\delta_t^3/(\kappa\nu)$, where ΔT_t is the temperature difference imposed over δ_t . As shown in figure 11, δ_t and ΔT_t change along the streamwise direction, and these changes eventually result in an increase or decrease of Ra_t . Once Ra_t exceeds the critical value, the confining effect will support the formation of a secondary flow at the top-lateral corners following the same scenario as that in RBP convection. This corner roll formation will occur irrespective of the onset of Rayleigh–Bénard-like convection, as shown in figure 4(a), i.e. weak rolls are formed even in a Q2-D state. The characteristic length of this initial secondary circulation depends on δ_s , the thickness of the downstream flow and the apparent Rayleigh number of the LRSs is $Ra_s = g\alpha\Delta T_s\delta_s^3/(\kappa\nu)$, where ΔT_s is the temperature difference imposed over δ_s . This roll formation progresses towards the interior and the downstream directions. Unlike the RBP convection, the secondary flow on the lateral walls is always downward because of the surface and the spanwise confinement. This regulates the spinning direction (or the sign of vorticity) of the LRSs formed upstream (see figure 5). Such LRSs are stable over time. A significant difference between RBP convection and SHC is their lower boundary. In the latter case, the bottom boundary is open, leading to spatial changes in the characteristics of LRSs. In figure 12(c), particle pathline images at two different x positions for the case of the 3-D state ($Pe = 5.5 \times 10^4$ and $Ri = 0.027$) are shown. Since the images are compiled using the colour images of the TLC particles, the colour qualitatively indicates the temperature fields, where blue is hot and red is cold. In the left panel, there are corner rolls at the top boundaries and the rest is stably stratified. In the right panel, reddish or greenish cold fluids are transported from the top and the LRSs occupy the whole spanwise domain, while the rest maintains stratification. The downstream region has thicker LRSs than the upstream region, as explained above.

Inspired by the RBP convection system described above, we examine a set of streamwise flow parameters to characterise the properties of the overturning circulation. Figure 13 displays δ_s/H and δ_t/H , $\Delta T_s/\Delta\theta$ and $\Delta T_t/\Delta\theta$, Ra_s and Ra_t and the number of rolls N_{roll} along the streamwise direction, x/W , for three Péclet numbers. Panels (a,d,g,j) show a Q2-D state with $Pe = 7.2 \times 10^3$ and $Ri = 80$. In contrast, panels (b,e,h,k) and (c,f,i,l) illustrate 3-D state cases with $Pe = 3.7 \times 10^4$ and $Ri = 0.293$, and $Pe = 5.5 \times 10^4$ and $Ri = 0.027$, respectively. Figure 13(a–c) shows δ_s/H and δ_t/H ; the results show that both δ_s and δ_t thicken downstream, almost monotonically, for the higher Pe cases.

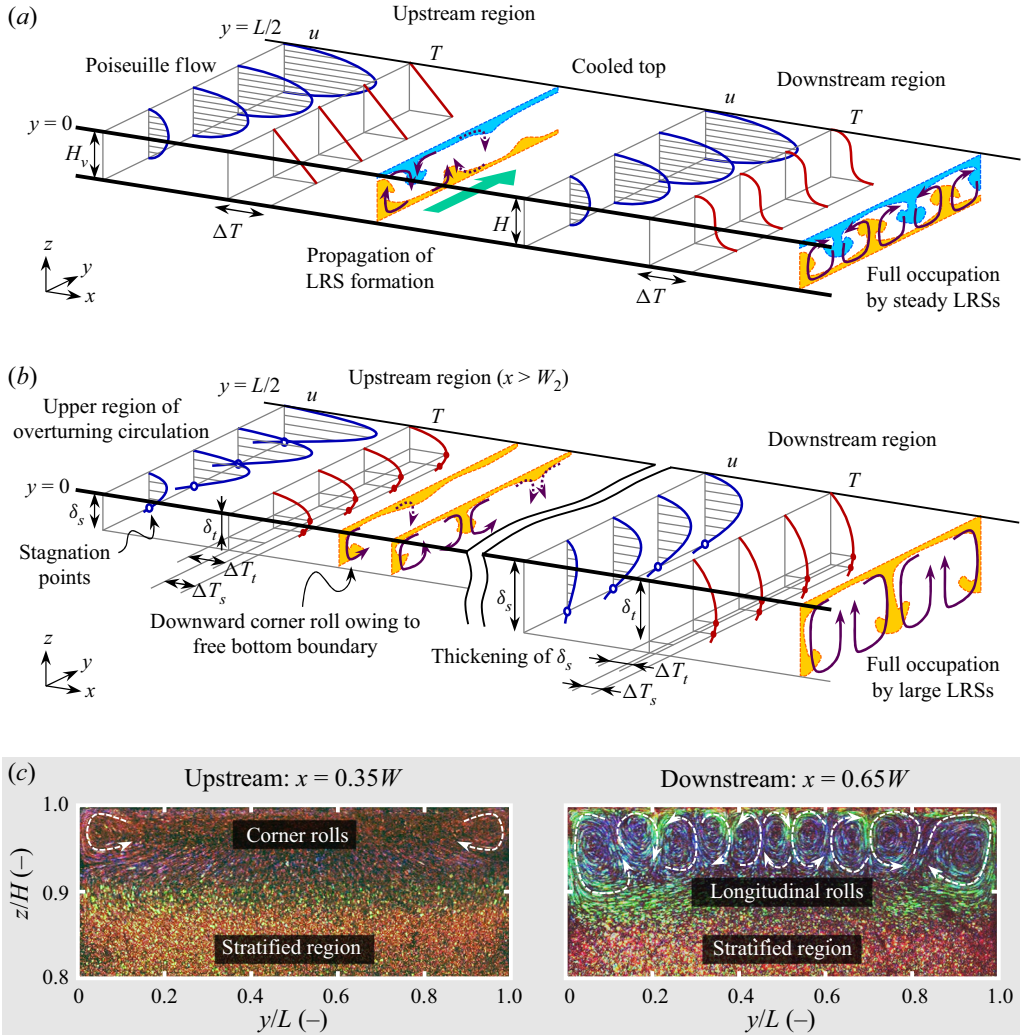


Figure 12. Schematic illustrations of LRS formation mechanism in (a) RBP convection and (b) SHC, and (c) colour particle pathline images of the TLC particles showing the LRS formations at different x positions ($Pe = 5.5 \times 10^4$ and $Ri = 0.027$). The colour in (c) qualitatively indicates the temperature distribution, and the flow directions are indicated by the arrows.

Figure 13(d–f) shows the vertical temperature differences $\Delta T_s/\Delta\theta$ and $\Delta T_t/\Delta\theta$. For the Q2-D state shown in figure 13(a,d,g,j), ΔT_t becomes positive in a highly limited region immediately after $x = W_2$, and ΔT_s is always negative. The latter implies that the system is mostly stably stratified over δ_s . On the other hand, ΔT_t and Δ_s become positive at $x > W_2$ for the 3-D state cases shown in figures 13(b,e,h,k) and (c,f,i,l). Such unstable temperature distributions decay gradually downstream.

We compute and plot the local Rayleigh numbers, Ra_s and Ra_t , as a function of x/W in figure 13(g–i). For reference, the critical Rayleigh numbers for the case of no-slip boundaries, $Ra_{cn} = 1708$, and free-slip boundaries, $Ra_{cf} = 657.5$ (Chandrasekhar 1961; Cross & Hohenberg 1993), are denoted by the dashed-dotted and dotted lines, respectively. For the 2-D case, Ra_t does not exceed the critical values. By contrast, for the 3-D state

Stratified horizontal convection

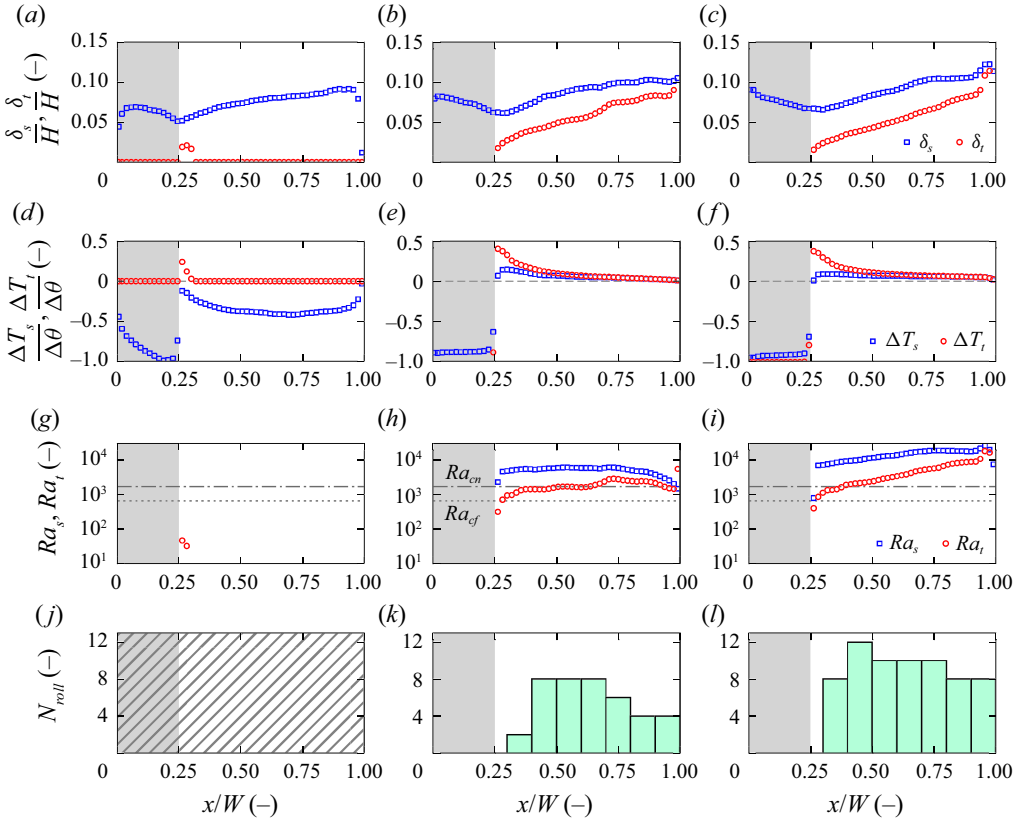


Figure 13. Streamwise-dependent features of RBP convection for different Pe conditions: (a,d,g,j) $Pe = 7.2 \times 10^3$, (b,e,h,k) $Pe = 3.7 \times 10^4$ and (c,f,i,l) $Pe = 5.5 \times 10^4$. Thicknesses of the downstream region δ_s and the unstable layer δ_t , local vertical temperature difference ΔT_s and ΔT_t , local Rayleigh number Ra_s and Ra_t and the number of LRSs N_{roll} are shown respectively from top to bottom. Grey regions, $x/W < 0.25$, correspond to the heated regions with a surface temperature of T_2 . Dashed-dotted lines and dotted lines correspond to critical Rayleigh numbers for no-slip Ra_{cn} and free-slip conditions Ra_{cf} , respectively. The values of N_{roll} are not available for (a,d,g,j) because of the absence of LRSs.

cases, Ra_t typically starts around 10^3 at $x \sim W_2$ which is quite close to the critical values. This result indicates that the formation of the LRSs is associated with the critical Rayleigh numbers. The critical Rayleigh number Ra_c is expressed as

$$Ra_c = \frac{g\alpha\Delta\theta\delta_c^3}{\nu\kappa} = \frac{Pe_c^2}{Pr} \frac{\delta_c^3}{hW^2}, \quad (5.1)$$

where δ_c is the minimum thickness corresponding to the potential maximum vertical temperature difference $\Delta\theta$. Here, Pe_c is the critical Péclet number for the onset of Rayleigh–Bénard-like convection. Accordingly, Pe_c can be expressed as

$$Pe_c = \left(Pr Ra_c \frac{hW^2}{\delta_c^3} \right)^{1/2}. \quad (5.2)$$

Assuming that $Ra_c \sim 10^3$ and $\delta_c \approx \delta_t$, Pe_c can be estimated from the experimental results. Even though δ_t changes with x , it varies approximately in the range 1–5 mm. Using these values, Pe_c is estimated as $Pe_c \gtrsim 10^4$, which is consistent with the empirical critical values

$Pe_c \approx 3.3 \times 10^4$ shown in figure 7. This consistency supports the above explanation that LRSs originated from Rayleigh–Bénard convection. The apparent Rayleigh number Ra_s of the LRSs ranges in $O(10^3\text{--}10^4)$, meaning that the downstream region maintains the supercriticality. For the case shown in figure 13(b,e,h,k), the Péclet number is marginally bigger than its critical empirical value for which SHC transitions from a Q2-D flow to a 3-D flow. In this case, Ra_s remains supercritical and almost uniform along x . However, for the case with the greatest Pe , shown in figure 13(c,f,i,l), Ra_s has a quasi-linear increase.

Figure 13(j–l) shows the number of LRSs N_{roll} in the y – z planes. the value of N_{roll} is zero in the region $0 \leq x/W \leq 0.25$, and the first pair of LRSs emerges from the lateral boundaries downstream $x > W_2$. The LRS formation propagates towards the interior, making N_{roll} increase until the spanwise domain is fully occupied by LRSs. The full development of LRSs is achieved at $x/W \sim 0.5$. After the full development, the LRSs start to merge with each other and this trend appears as the decrease of N_{roll} . The coalescence keeps the aspect ratio of the LRSs almost constant, not far from unity, over the whole downstream region, as the roll regions are thickening downstream.

Summing up, the streamwise dependent features shown in figure 13 provide robust evidence that LRSs developed in SHC obey analogue physical processes to those controlling the transition to 3-D flow in RBP convection: it is a localised phenomenon that spontaneously happens at high- Pe conditions ($Pe \gtrsim 3.3 \times 10^4$), leading to supercritical Ra_t , that support (i) local heat transport via Rayleigh–Bénard-like convection, (ii) the vertical expansion of the overturning circulation and (iii) ultimately the enhancement of the horizontal transport.

5.2. Mechanical energy conversion

As shown in figure 9, only a small portion of the APE is converted into KE in SHC. The latter implies that SHC is a system in which most of the available energy is utilised in sustaining the stratification and mixing of the overturning region. To quantify the mechanical energy conversion, we diagnose the mixing efficiency η defined as $\eta = (\Phi_d - \Phi_i)/(\Phi_d - \Phi_i + \epsilon)$ (Peltier & Caulfield 2003). Here, $\Phi_d = -\kappa g \int_V (dz_*/d\rho) |\nabla \rho|^2 dV$ is the rate at which E_{ap} depletes due to the irreversible scalar mixing controlling ρ and $\Phi_i = -\kappa g WL(\rho_{top} - \rho_{bottom})$ is the conversion rate from internal energy to PE, where ρ_{top} and ρ_{bottom} are the laterally averaged densities at the top and the bottom boundaries, respectively (Winters *et al.* 1995). Also, $\epsilon = \rho_0 \nu \int_V (|\nabla u|^2 + |\nabla v|^2 + |\nabla w|^2) dV$ is the KE dissipation rate. Irrespective of the conditions, we obtained $\eta \approx 0.99$, close to unity. Please note that the density (temperature) fields are reconstructed under 2-D assumption (4.6), and the energy budget of the system is not fully closed. Hence, one can expect that our estimation of η may differ from systems that fully close the energy budget. In HC systems, $\eta \rightarrow 1$ is predicted theoretically as an upper bound for the inviscid regime with very large Ra (Scotti & White 2011), whereas numerical simulation shows a slightly smaller value, $\eta = 0.923$ (Gayen *et al.* 2013).

Considering the difference in the effective lower boundary of the overturning circulation in SHC (stably stratified layer) and HC (no-slip wall boundary), one would expect SHC to develop less viscous dissipation than HC. In SHC, the lower stably stratified layer acts as an adjustable ‘soft no-slip’ boundary, unlike the rigid no-slip bottom set in HS, in which a vigorous flow has no other option than to intensify its shear rate rather than mix and expand as in the case of SHC. Despite this fundamental difference, the estimated mixing efficiency for SHC remains in close agreement with values obtained through numerical simulations and upper bound scalings for HC.

6. Concluding remarks

This paper investigated experimentally the fluid dynamics of SHC, the overturning circulations driven by surface differential heating in stably stratified fluid bodies. The designed experimental framework allowed us to measure the quasi-instantaneous 3-D velocity field by utilising multiple cameras and scanning light blade systems. Moreover, from the measured velocity field and prescribed boundary conditions, we reconstructed the Q2-D temperature field that fulfils the steady state momentum balance achieved in the experiments.

SHC can be described by the Rayleigh number Ra , representing the destabilising effect of buoyancy, and the bulk Richardson number Ri , representing the stabilising effect of background stratification. We derived a characteristic length scale from the system's parameters which predicts the overturning circulation thickness and its characteristic velocity U_{adv} by accounting for the hypothetical equilibrium height of fluid parcels. From these scales, we define the Péclet number, $Pe = U_{adv}W/\kappa = [(Pr Ra)/(\mathcal{A} Ri \Theta)]^{1/2}$, which consolidates all the dimensionless parameters involved in SHC, including the vertical and horizontal temperature difference ratio Θ , the basin aspect ratio \mathcal{A} and the Prandtl number Pr in addition to Ra and Ri .

We observed experimentally the fluid dynamics of SHC, the formation of a Q2-D overturning circulation confined at the upper region above the stably stratified layer and its transition towards 3-D LRSs. Here, we show theoretically and experimentally that Pe governs the global properties, such as the maximum streamfunction $\psi_{max} \propto Pe$ and the available mechanical energy of the system. Furthermore, we showed that local properties, such as the flow dimensionality, are ruled by Pe . We also discussed mechanical energy conversion, finding that the irreversible mixing of SHC is extremely high, in agreement with the theoretical and numerical results of HC.

In conclusion, our study provides insights into stratified fluid environments that experience horizontal density gradients, such as lakes, oceans and atmospheres. There is a wide range of aspects that future research could explore via theoretical studies, laboratory experiments and numerical simulations, for instance: (i) the conditions for developing secondary LRS; (ii) the transition towards turbulence, potentially at higher Pe ; (iii) the system response to different Pr and \mathcal{A} ; (iv) the effects of lateral confinements; and (v) the impact of rotation.

Acknowledgements. The authors are grateful for the helpful discussions with Dr T. Miyagoshi (Japan Agency for Marine-Earth Science and Technology, JAMSTEC). The authors also thank the anonymous reviewers for encouraging and constructive comments. D.N. and H.N.U. acknowledge the support of the Start-up fund at the Department of Earth and Environmental Science, University of Pennsylvania.

Fundings. This work was partially supported by the Grant-in-Aid for the Japan Society for the Promotion of Science (JSPS) Fellows (grant no. 19JP19006).

Declaration of interests. The authors report no conflict of interest.

Author ORCIDs.

 Daisuke Noto <https://orcid.org/0000-0003-3713-4777>;

 Hugo N. Ulloa <https://orcid.org/0000-0002-1995-6630>;

 Takatoshi Yanagisawa <https://orcid.org/0000-0001-6289-938X>;

 Yuji Tasaka <https://orcid.org/0000-0002-8943-4803>.

REFERENCES

- AKIYAMA, M., HWANG, G.J. & CHENG, K.C. 1971 Experiments on the onset of longitudinal vortices in laminar forced convection between horizontal plates. *Trans. ASME J. Heat Transfer* **93** (4), 335–341.
- ANDERS, S., NOTO, D., TASAKA, Y. & ECKERT, S. 2020 Simultaneous optical measurement of temperature and velocity fields in solidifying liquids. *Exp. Fluids* **61**, 113.
- CHANDRASEKHAR, S. 1961 *Hydrodynamic and Hydromagnetic Stability*. Dover.
- CHIU-WEBSTER, S., HINCH, E.J. & LISTER, J.R. 2008 Very viscous horizontal convection. *J. Fluid Mech.* **611**, 395–426.
- COATES, M.J. & PATTERSON, J.C. 1993 Unsteady natural convection in a cavity with non-uniform absorption of radiation. *J. Fluid Mech.* **256**, 133–161.
- COMAN, M.A., GRIFFITHS, R.W. & HUGHES, G.O. 2006 Sandström’s experiments revisited. *J. Mar. Res.* **64** (6), 783–796.
- COUSTON, L.-A., NANDAHA, J. & FAVIER, B. 2022 Competition between Rayleigh–Bénard and horizontal convection. *J. Fluid Mech.* **947**, A13.
- CROSS, M.C. & HOHENBERG, P.C. 1993 Pattern formation outside of equilibrium. *Rev. Mod. Phys.* **65** (3), 851.
- DAILEY, P.S. & FOVELL, R.G. 1999 Numerical simulation of the interaction between the sea-breeze front and horizontal convective rolls. Part I. Offshore ambient flow. *Mon. Weath. Rev.* **127** (5), 858–878.
- GAYEN, B. & GRIFFITHS, R.W. 2022 Rotating horizontal convection. *Annu. Rev. Fluid Mech.* **54**, 105–132.
- GAYEN, B., GRIFFITHS, R.W. & HUGHES, G.O. 2014 Stability transitions and turbulence in horizontal convection. *J. Fluid Mech.* **751**, 698–724.
- GAYEN, B., GRIFFITHS, R.W., HUGHES, G.O. & SAENZ, J.A. 2013 Energetics of horizontal convection. *J. Fluid Mech.* **716**, R10.
- GILLE, S.T., LLEWELLYN, S., STEFAN, G. & STATOM, N.M. 2005 Global observations of the land breeze. *Geophys. Res. Lett.* **32**, L05605.
- GRAMBERG, H.J.J., HOWELL, P.D. & OCKENDON, J.R. 2007 Convection by a horizontal thermal gradient. *J. Fluid Mech.* **586**, 41–57.
- HUGHES, G.O. & GRIFFITHS, R.W. 2008 Horizontal convection. *Annu. Rev. Fluid Mech.* **40**, 185–208.
- ILICAK, M. & VALLIS, G.K. 2012 Simulations and scaling of horizontal convection. *Tellus A* **64** (1), 18377.
- LEMONE, M.A. 1973 The structure and dynamics of horizontal roll vortices in the planetary boundary layer. *J. Atmos. Sci.* **30** (6), 1077–1091.
- LU, J., ARYA, S.P., SNYDER, W.H. & LAWSON JR, R.E. 1997a A laboratory study of the urban heat island in a calm and stably stratified environment. Part I. Temperature field. *J. Appl. Meteorol.* **36a** (10), 1377–1391.
- LU, J., ARYA, S.P., SNYDER, W.H. & LAWSON, R.E. 1997b A laboratory study of the urban heat island in a calm and stably stratified environment. Part II. Velocity field. *J. Appl. Meteorol.* **36** (10), 1392–1402.
- MAO, Y., LEI, C. & PATTERSON, J.C. 2009 Unsteady natural convection in a triangular enclosure induced by absorption of radiation—a revisit by improved scaling analysis. *J. Fluid Mech.* **622**, 75–102.
- MERGUI, S., NICOLAS, X. & HIRATA, S. 2011 Sidewall and thermal boundary condition effects on the evolution of longitudinal rolls in Rayleigh–Bénard–Poiseuille convection. *Phys. Fluids* **23** (8), 084101.
- MONISMITH, S.G., GENIN, A., REIDENBACH, M.A., YAHIEL, G. & KOSEFF, J.R. 2006 Thermally driven exchanges between a coral reef and the adjoining ocean. *J. Phys. Oceanogr.* **36** (7), 1332–1347.
- MORI, A. & NIINO, H. 2002 Time evolution of nonlinear horizontal convection: its flow regimes and self-similar solutions. *J. Atmos. Sci.* **59** (11), 1841–1856.
- MULLARNEY, J.C., GRIFFITHS, R.W. & HUGHES, G.O. 2004 Convection driven by differential heating at a horizontal boundary. *J. Fluid Mech.* **516**, 181–209.
- NICOLAS, X. 2002 Bibliographical review on the Poiseuille–Rayleigh–Bénard flows: the mixed convection flows in horizontal rectangular ducts heated from below. *Intl J. Therm. Sci.* **41** (10), 961–1016.
- NIINO, H., MORI, A., SATOMURA, T. & AKIBA, S. 2006 Flow regimes of nonlinear heat island circulation. *J. Atmos. Sci.* **63** (5), 1538–1547.
- NOTO, D., TASAKA, Y., YANAGISAWA, T. & MURAI, Y. 2019 Horizontal diffusive motion of columnar vortices in rotating Rayleigh–Bénard convection. *J. Fluid Mech.* **871**, 401–426.
- NOTO, D., TERADA, T., YANAGISAWA, T., MIYAGOSHI, T. & TASAKA, Y. 2021 Developing horizontal convection against stable temperature stratification in a rectangular container. *Phys. Rev. Fluids* **6** (8), 083501.
- NOTO, D., ULLOA, H.N. & LETELIER, J.A. 2023 Reconstructing temperature fields for thermally-driven flows under quasi-steady state. *Exp. Fluids* **64** (4), 74.
- PABIOU, H., MERGUI, S. & BENARD, C. 2005 Wavy secondary instability of longitudinal rolls in Rayleigh–Bénard–Poiseuille flows. *J. Fluid Mech.* **542**, 175–194.

- PASSAGGIA, P.-Y., SCOTTI, A. & WHITE, B. 2017 Transition and turbulence in horizontal convection: linear stability analysis. *J. Fluid Mech.* **821**, 31–58.
- PELTIER, W.R. & CAULFIELD, C.P. 2003 Mixing efficiency in stratified shear flows. *Annu. Rev. Fluid Mech.* **35** (1), 135–167.
- ROSSBY, H.T. 1965 On thermal convection driven by non-uniform heating from below: an experimental study. In *Deep-Sea Res.*, vol. 12, pp. 9–16. Elsevier.
- SARRIS, I.E., LEKAKIS, I. & VLACHOS, N.S. 2002 Natural convection in a 2D enclosure with sinusoidal upper wall temperature. *Numer. Heat Transfer A* **42** (5), 513–530.
- SCHNEIDER, T. 2006 The general circulation of the atmosphere. *Annu. Rev. Earth Planet. Sci.* **34**, 655–688.
- SCOTTI, A. & WHITE, B. 2011 Is horizontal convection really “non-turbulent?”. *Geophys. Res. Lett.* **38**, L21609.
- SHISHKINA, O., GROSSMANN, S. & LOHSE, D. 2016 Heat and momentum transport scalings in horizontal convection. *Geophys. Res. Lett.* **43** (3), 1219–1225.
- TAHER, R. & ABID, C. 2018 Experimental determination of heat transfer in a Poiseuille–Rayleigh–Bénard flow. *Heat Mass Transfer* **54** (5), 1453–1466.
- TAHER, R., AHMED, M.M., HADDAD, Z. & ABID, C. 2021 Poiseuille–Rayleigh–Bénard mixed convection flow in a channel: heat transfer and fluid flow patterns. *Intl J. Heat Mass Transfer* **180**, 121745.
- TERADA, T., NOTO, D., TASAKA, Y., MIYAGOSHI, T. & YANAGISAWA, T. 2023 Structural variety of developing and equilibrium horizontal convection confined in a rectangular vessel resulting from different heating plate arrangements. *J. Vis.* doi:10.1007/s12650-023-009.
- TSENG, Y. & FERZIGER, J.H. 2001 Mixing and available potential energy in stratified flows. *Phys. Fluids* **13** (5), 1281–1293.
- ULLOA, H.N., RAMÓN, C.L., DODA, T., WÜEST, A. & BOUFFARD, D. 2022 Development of overturning circulation in sloping waterbodies due to surface cooling. *J. Fluid Mech.* **930**, A18.
- VERBURG, P., ANTENUCCI, J.P. & HECKY, R.E. 2011 Differential cooling drives large-scale convective circulation in Lake Tanganyika. *Limnol. Oceanogr.* **56** (3), 910–926.
- VILA, C.S., DISCETTI, S., CARLOMAGNO, G.M., ASTARITA, T. & IANIRO, A. 2016 On the onset of horizontal convection. *Intl J. Therm. Sci.* **110**, 96–108.
- WALSH, J.E. 1974 Sea breeze theory and applications. *J. Atmos. Sci.* **31** (8), 2012–2026.
- WANG, W. & HUANG, R.X. 2005 An experimental study on thermal circulation driven by horizontal differential heating. *J. Fluid Mech.* **540**, 49–73.
- WANG, F., HUANG, S.-D. & XIA, K.-Q. 2018 Contribution of surface thermal forcing to mixing in the ocean. *J. Geophys. Res. Oceans* **123** (2), 855–863.
- WECKWERTH, T.M., WILSON, J.W. & WAKIMOTO, R.M. 1996 Thermodynamic variability within the convective boundary layer due to horizontal convective rolls. *Mon. Weath. Rev.* **124** (5), 769–784.
- WINTERS, K.B. & BARKAN, R. 2013 Available potential energy density for Boussinesq fluid flow. *J. Fluid Mech.* **714**, 476–488.
- WINTERS, K.B., LOMBARD, P.N., RILEY, J.J. & D’ASARO, E.A. 1995 Available potential energy and mixing in density-stratified fluids. *J. Fluid Mech.* **289**, 115–128.
- WUNSCH, C. & FERRARI, R. 2004 Vertical mixing, energy, and the general circulation of the oceans. *Annu. Rev. Fluid Mech.* **36**, 281–314.